PDAVIS: Bio-inspired Polarization Event Camera

Germain Haessig[1,2,†], Damien Joubert[2,3,†], Justin Haque[4,†], Moritz B. Milde[2,3], Tobi Delbruck[2,*], and Viktor Gruev[4,*]

[1]AIT Austrian Institute of Technology, Center for Vision, Automation & Control, High-performance Vision Systems, Vienna, Austria
[2]Institute of Neuroinformatics, University of Zurich and ETH Zurich, Switzerland
[3]International Centre for Neuromorphic Systems, The MARCS Institute, Western Sydney University, Sydney, Australia
[4]Department of Electrical and Computer Engineering, University of Illinois at Urbana-Champaign, Urbana, IL, USA
[†]These authors contributed equally
[*]Contact authors emails: tobi@ini.uzh.ch, vgruev@illinois.edu

Abstract

The stomatopod (mantis shrimp) visual system has recently provided a blueprint for the design of paradigm-shifting polarization and multispectral imaging sensors, enabling solutions to challenging medical and remote sensing problems. However, these bioinspired frame-based cameras lack the high dynamic range and asynchronous polarization vision capabilities of the stomatopod visual system, limiting temporal resolution to ∼12 ms and dynamic range to ∼72 dB. Here we present a novel stomatopod-inspired polarization camera which mimics the sustained and transient biological visual pathways to save power and sample data beyond the maximum Nyquist frame rate. This bio-inspired sensor simultaneously captures both synchronous intensity frames and asynchronous polarization brightness change information with submillisecond latencies over a million-fold range of illumination. Our PDAVIS camera is comprised of 346x260 pixels, organized in 2-by-2 macropixels, which filter the incoming light with four linear polarization filters offset by 45°. Polarization information is reconstructed using both low-cost and low-latency event-based algorithms and more accurate but slower deep neural networks. Our sensor is used to image high dynamic range polarization scenes that vary at high speeds and to observe the dynamical properties of single collagen fibers in a bovine tendon under rapid cyclical loads.

Video: https://youtu.be/mFuCeTMWEqY

1. Introduction

Visual information is encoded in light by intensity, color, and polarization [1]. This information is sensed by biological eyes [1]–[3] and artificial cameras [4]–[10] which each have been optimized by evolution driven by maximum fitness. Eyes have evolved to support visually guided behavior for the benefit of survival, while digital cameras have mainly evolved to supply consumer demand for high-resolution photography. These different evolutionary paths have created very different visual systems. Existing spectral and polarization digital cameras use synchronous and generally redundant frames with linear photo response [5], [9], [11]–[14]. By contrast, eyes are asynchronous, have a compressed nonlinear response, and their output is sparse and highly informative [1].

The mantis shrimp visual system (Fig. 1a) is considered one of the most sophisticated visual systems in nature. It is sensitive to more than 12 spectral, 4 linear, and 2 circular polarization channels [1], [2]. Its photosensitive microvilli have a logarithmic high dynamic range (**HDR**) response to incident light. Sensitivity to linearly polarized light is in part expressed in the dorsal and ventral parts of the ommatidia, where individual photoreceptors are comprised of orthogonal sets of microvilli sensitive to orthogonal polarization states. The dorsal/ventral views largely overlap, and since the dorsal and ventral microvilli are offset by 45°, four linear polarization states offset by 45° are captured by the eye. The logarithmic photo responses of the microvilli enable high dynamic range polarization sensing capabilities, while their asynchronous response to temporally varying brightness greatly reduces the visual information that is transmitted to their brain for further processing. It is believed that mantis shrimp use polarization to discriminate short-range prey [1], to select a mating partner [15] and to orient during short-range navigation using celestial polarization patterns [16].

Our work capitalizes on the development of bioinspired neuromorphic vision sensors, which have enabled higher dynamic range and lower latency machine vision [17], [18].

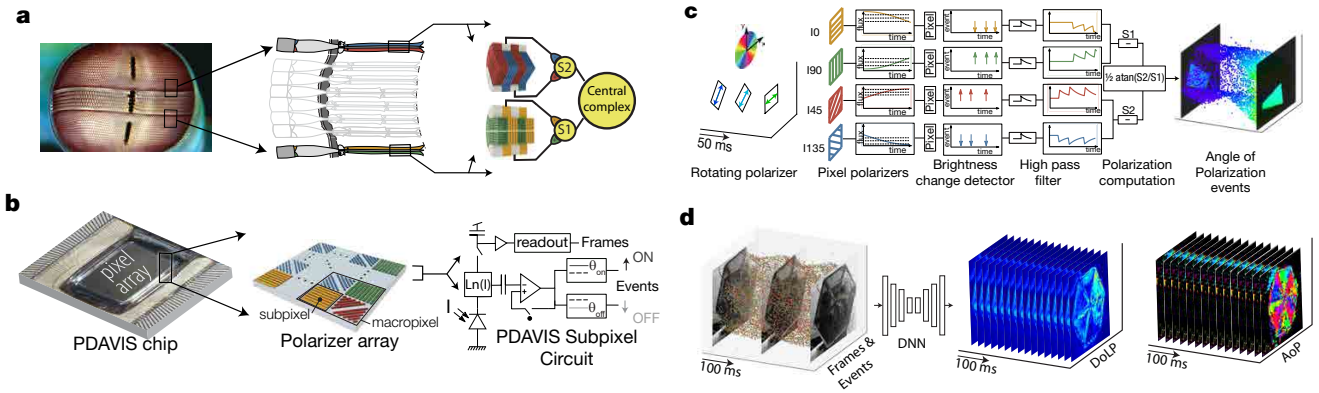

Figure 1. **Overview of our bio-inspired Polarization Dynamic and Active pixel VIsion Sensor (PDAVIS). (a)** Polarization vision in the mantis shrimp eye (left) is in part enabled by two sets of orthogonal microvilli located in the dorsal and ventral hemisphere (center), capturing total of 4 linear polarization states offset by 45 degrees (right). This polarization sensitivity paired with logarithmic photoreceptors that output only brightness change enable the mantis shrimp to be effective predator in the shallow coral reefs [1]. **(b)** The PDAVIS polarization event camera (left), effectively mimics the mantis shrimp eye by integrating an array of pixelated polarization filters offset by 45 degrees (center, angle indicated by false colors) with a vision sensor that provides both sustained pathway frames and transient pathway log-scale brightness change events (right) (see Sup. Mat. 1). **(c)** A rectangular rotating linear polarizer (left) generates a stream of brightness change events from the four subpixels in the PDAVIS macropixels that see the polarizer (center). A temporal filter approximates the temporal derivative from the four individual pixels and then computes the Angle of Polarization (**AoP**). The result is a stream of AoP events with low latency (right). (see 3.2). **(d)** A polarization filter wheel is rotated in front of PDAVIS, which produces frames and events (left) represented in false colors shown in (c). A DNN (center-left) reconstructs DoLP (center-right) and AoP (right) from the brightness change events at a higher rate than the cameras maximum frame rate (see 3.4).

Inspired by the ommatidia of mantis shrimp, individual PDAVIS subpixel circuits [17] are each overlaid with one of four pixelated linear polarization filters (Fig. 1b). The PDAVIS takes inspiration from biology by saving energy by partitioning the perception of fine detail and fast motion into sustained and transient pathways [1]. It provides a relatively low frequency synchronous readout of frames like conventional cameras (the "sustained" pathway), and it concurrently outputs a high frequency stream of asynchronous brightness change events (the "transient" pathway). Each event represents a signed log intensity change. Pixels that see more brightness change generate more events, and the events have sub-millisecond temporal resolution driven by the dynamics of the scene. The events enable reconstructing the absolute intensity between the synchronous frame intensity samples.

2. Related Work

Current polarization imaging sensors are categorized into several types, including division of time, division of amplitude, division of aperture, and Division of Focal Plane (**DoFP**) polarimeters [19]–[21]. One of the earliest methods of polarization imaging used CMOS or CCD imaging sensors with electrically or mechanically controlled polarization filters, known as division of time polarimeters. These systems sampled the environment with at least three polarization filters. However, they have several drawbacks, such as reducing the frame rate by a factor of three, high power consumption, and errors due to motion during sampling. Motion blur effects have been partially addressed by combining event-based cameras with rotating polarization filters to enable 3d shape reconstruction [22].

DoFP polarimeters use imaging and micropolarization filters on the same substrate to sample the environment with spatially distributed micropolarization filters. Birefringent materials and thin film polarizers have been used to incorporate pixel-pitch-matched polarization filters at the focal plane [5], [23]–[26]. The monolithic integration of pixelated filters and imaging elements have produced compact, low power, snap-shot polarimeters that have enabled many challenging applications [5], [14]. Despite vigorous research in single-chip polarization cameras, the current state-of-the-art polarization sensors are frame-based, which have limited dynamic range and frame rates.

3. Reconstructing Polarization Information

3.1. Conventional Polarization Imaging

Polarization is commonly described using the Stokes parameters: (S_0, S_1, S_2) defined [27]:

$$S_0(t) = I_0(t) + I_{90}(t) \quad (1)$$

$$S_1(t) = I_0(t) - I_{90}(t) \quad (2)$$

$$S_2(t) = I_{45}(t) - I_{135}(t) \quad (3)$$

where I_i stands for the light intensity transmitted by the linear polarizer filter with angle i. A fourth Stokes parameter $(S3)$ describes the circular polarization properties of

the light field, which is not detected by the PDAVIS sensor. The Degree of Linear Polarization (**DoLP**), which described how much light is polarized, and the AoP, which describes the dominant axis of light's oscillation, can then be estimated from the Stokes parameters:

$$\text{DoLP}(t) = \frac{\sqrt{S_1(t)^2 + S_2(t)^2}}{S_0(t)} \tag{4}$$

$$\text{AoP}(t) = \frac{1}{2}\arctan\left(\frac{S_2(t)}{S_1(t)}\right) \tag{5}$$

3.2. Reconstructing AoP from PDAVIS events only

We can reconstruct the change in absolute log intensity dL from an arbitrary starting point by simply integrating the events over time, as first studied experimentally by Brandli, Muller, and Delbruck [28]. Pixel nonidealities cause this estimate to drift. The *events* method regards the events as providing high frequency information about the log intensity change[29]. Above a corner frequency $f_{3\text{dB}} = 2\pi\omega = 1/(2\pi\tau)$, the events directly update the filtered log intensity estimate, which decays to zero with time constant τ between events. Since the AoP depends only on ratios of differences of I_i values, the absolute intensity factors out, so we can compute AoP from the reconstructed I_i values.

For every incoming event, the *events* method asynchronously updates the related reconstructed log intensity change $dL = d\log(F)$ as the asynchronous first-order Infinite Impulse Response (**IIR**) filter (6):

$$\begin{aligned} \alpha &\leftarrow e^{-\Delta t/\tau} \\ dL &\leftarrow \alpha dL + p \end{aligned} \tag{6}$$

where Δt is the time elapsed since last event from the subpixel, τ is the filter time constant, and $p = [+\theta_{\text{on}}, -\theta_{\text{off}}]$ is the signed event threshold, which we estimate from the known bias currents using the formulas from Nozaki and Delbruck [30] and then fine tune to match the low frequency frame-based data.

From the dL values, we can compute AoP by exponentiation of dL to obtain the subpixel I_i value, and use the resulting I_i values in (5). In practice, we use the dL values directly, since generally $|dL| < 1$ and thus $\exp(dL) \approx 1 + dL$. The 1 would be the same for all terms in (5) and would thus cancel, leaving the dL value.

The dL in (6) is the highpass-filtered log intensity, corresponding to the Laplace domain transfer function (7):

$$H_{\text{dL}}(s) \equiv \frac{dL(s)}{\sum p(s)} = \frac{\tau s}{1 + \tau s} \tag{7}$$

where s is the complex frequency, and $\sum p$ is the staircase sum of Dirac delta brightness changes since filter startup.

There are two exactly equivalent descriptions of this filter: dL is a highpass-filtered log intensity, and it is also a lowpass-filtered derivative of log intensity. Thus, for frequencies well below the $f_{3\text{dB}}$ corner frequency $dL \approx \tau dL/dt$, *i.e.*, dL can be considered as a lowpass filtered derivative of L, which filters out derivatives above $f_{3\text{dB}}$. For frequencies well above $f_{3\text{dB}}$, dL is equal to L minus its DC value averaged over the exponential time window τ. If we can assume that this offset is equivalent for each subpixel, then it cancels out in S_1 and S_2, which are used to compute the AoP. For the *events* results in 2 we used $f_{3\text{dB}} = 0.5$ Hz.

Effect of high pass filter on AoP: For input frequencies well above $f_{3\text{dB}}$, using the dL values in (5) results in the AoP if we make the reasonable assumption that all I_x have the same mean value. For frequencies below $f_{3\text{dB}}$, where $dL \approx \tau dL/dt$, the following computation shows that using dL in the AoP equation (5) results in the AoP, but with a phase shift of $\pi/4$. First, we use the modulated intensit to compute the derivative of I_i, where i is one of the polarizer angles:

$$\frac{\partial I_i(t)}{\partial t} = -2I_t\text{DoLP}(t)\frac{\partial\theta(t)}{\partial t}\sin\left[\theta(t) - i\right]\cos\left[\theta(t) - i\right] \tag{8}$$

Since we only care about measuring a varying AoP, we have assumed that DoLP and I_t are constant. Now we can plug (8) into (5):

$$\begin{aligned} \frac{1}{2}\arctan\left(\frac{\partial S_2/\partial t}{\partial S_1/\partial t}\right) = \\ &= \frac{1}{2}\arctan\left(\frac{\partial I_{45}/\partial t - \partial I_{135}/\partial t}{\partial I_0/\partial t - \partial I_{90}/\partial t}\right) \\ &= \frac{1}{2}\arctan\left(\frac{2\sin(\theta - \frac{\pi}{4})\cos(\theta - \frac{\pi}{4})}{2\sin(\theta)\cos(\theta)}\right) \\ &= \frac{1}{2}\arctan\left(\frac{1}{-\tan(2\theta)}\right) \\ &= \theta(t) \bmod \pi + \frac{\pi}{4} \\ &= \text{AoP}(t) \bmod \pi + \frac{\pi}{4} \end{aligned} \tag{9}$$

According to (9), using the temporal derivatives of intensities in (5) results in the AoP with a (constant $\pi/4$) offset.

In practice, we used signal periodicity to estimate the AoP phase in Fig. 2. Most of our experiments used a stimulus frequency above $f_{3\text{dB}}$, so the output of the AoP from the events method corresponds to the actual AoP without this offset. For example, Fig. 2c shows the reconstructed AoP sawtooth at 30 RPM, corresponding to an AoP frequency of 1Hz, which is double the $f_{3\text{dB}} = 0.5$ Hz corner frequency.

The AoP values are updated as soon as each event is received, creating polarization events as illustrated in Fig. 1c. These asynchronous updates could drive a quick event-driven processing pipeline that exploits the precise timing of events. Source code for this algorithm is available [1].

3.3. Complementary Filter: Reconstructing AoP and DoLP by fusing frames and events

The Complementary Filter (**CF**) of Scheerlinck [29] is *complementary* because it considers Active Pixel Sensor (**APS**) frames as providing reliable low frequency intensity (albeit with limited Dynamic Range (**DR**)), while the Dynamic Vision Sensor (**DVS**) events provide reliable high frequency information about brightness (changes). The CF method fuses the high pass filtered log intensity of the events method with low pass filtered frames. At the CF crossover frequency $\omega = 1/\tau = 2\pi f_{3\text{dB}}$, the frame and event estimates of log intensity are weighted equally. For lower frequencies, the frame intensities are weighted more, and for higher frequencies, the event-based estimations are weighted more.

The CF also has a computational cost of about 10 operations per DVS event or APS sample, making it attractive for real-time applications.

At each subpixel, the CF updates its log intensity reconstruction L each time the pixel measures either intensity or generates a DVS event. The CF outputs the log intensity L from the most recent log intensity sample or DVS event. For each pixel's APS intensity sample or DVS event, the asynchronous first-order IIR filter CF update is

$$\begin{aligned} \alpha &\leftarrow e^{-\Delta t/\tau} \\ L &\leftarrow \underbrace{\alpha L + p}_{\text{DVS}} + \underbrace{(1-\alpha) L_{\text{aps}}}_{\text{APS}} \end{aligned} \tag{10}$$

where Δt is the time since last update, $\tau = 1/(2\pi f_{3\text{dB}})$ is the filter time constant, $p = [+\theta_{\text{on}}, -\theta_{\text{off}}]$ is the event's log intensity change, and L_{aps} is the log intensity sample. (If the update is for an event, $L_{\text{aps}} = 0$, or if the update is for a frame, $p = 0$.) Since $\Delta t \ll \tau$ (*i.e.*, the update rate is much higher than the time constant), $\alpha \approx 1 - \Delta t/\tau \sim 1$. Removing the APS input from Eq. 10 gives the *events* method presented in the previous section (Eq. 6).

In the Laplace domain, the CF filter has form (11):

$$L(s) = \frac{\tau s}{1+\tau s} \sum p(s) + \frac{1}{1+\tau s} L_{\text{APS}}(s). \tag{11}$$

For our experiments, we used CF $f_{3\text{dB}} = 1.6$ Hz. The AoP and DoLP are periodically computed using the subpixel L values.

Adaptive gain tuning: The CF method includes a down-weighting of the APS samples when L_{aps} approach their limits, *i.e.*, are under or overexposed [29, Sec. 4.1]. We used this feature to improve the DR of the reconstruction. We set adaptive gain tuning $\lambda = 0.1$ and used the limits $L_1, L_2 = \log(10, 200)$.

Filter startup: To avoid the CF filter startup transient, we initialize the filter output state to the first L_{APS} frame as soon as it is available.

Source code for the original CF implementation, our implementation of CF, and for computing PDAVIS polarization information are available[2].

3.4. Polarization FireNet: Reconstructing AoP and DoLP from events

The DNN method applied to the PDAVIS data is based on deep learning and infers the intensity sensed by each subpixel using only the brightness change events. It is based on the work of [31], [32], which showed that it is possible to train a deep recurrent neural network to reconstruct video purely from DVS brightness change events, as long as there is motion in the scene. The reconstructed offset level is chosen by the DNN based on the statistics of its training data samples since the DVS output transmits no offset information, but the reconstruction is locally more accurate in comparison to the CF method.

We used the pretrained *FireNet* [31] neural network. For the polarization reconstruction, the events are first separated into 4 channels, each corresponding to one pixel of 2-by-2 macropixels. Each channel represents one of four different polarization angles (see Sec. Sup. Mat. 1 and Fig. 1). The events are then accumulated into 3D tensors with the same predetermined exposure time window for each channel, which is different from the original *FireNet* which used constant event-count exposures. This binning requires that the necessary sample rate must be known a priori to obtain a precise reconstruction of the polarization information. To synchronize the four channels, we used a fixed time window in opposition to a fixed event count, because each channel codes for different and sometimes even orthogonal angles of polarization, hence emitting a different number of events. For example, in the DR measurement, the time window is set to 10 ms.

Once we receive the stack of frames from the *FireNet*, calibration is applied. For the data collected using only a linear polarizer (Fig. 2), we subtract an offset calculated by the minimum value of each of the 4 channels before calculating AoP. For the DoLP calculation, a gain table of

[1] https://github.com/joubertdamien/poladvs

[2] https://github.com/cedric-scheerlinck/dvs_image_reconstruction, https://github.com/SensorsINI/jaer/blob/master/src/ch/unizh/ini/jaer/projects/davis/frames/DavisComplementaryFilter.java, https://github.com/SensorsINI/jaer/blob/master/src/au/edu/wsu/PolarizationComplementaryFilter.java, https://github.com/joubertdamien/pyComplementaryFilter

the digital numbers paired with its respective multipliers is made for each RPM from one AoP cycle. This table gives us the non linear mapping from logarithmic to linear response for each of the four channels that is used on a second data set to calculate the corrected DoLP. As for the DoLP calculation of the data collected from the linear polarizer and quarter wave plate (Fig. 3), the 4 channels only have an offset and normalization of the max data point applied before DoLP calculation. Then, the *FireNet* outputs intensity frames from the event tensors, which we use to compute the angle and degree of polarization using Eqs. (5) and (4).

Our source code for *FireNet* reconstruction is available on GitHub[3].

4. Experimental Validation

First, we assessed the ability to reconstruct the time-varying AoP of fully linearly polarized light (with DoLP=1) by rotating a linear polarizer at constant speeds (Fig. 2, Sup. Mat. 1, Supplementary Figs. S2, Video). At low rotation speeds of less than 60 RPM, the AoP reconstruction error from both sensors is less than 5°, with the Sony sensor having the lowest reconstruction error. The reconstructed DoLP is nearly 1 from both sensors, as expected. Since Sony's polarization sensor is fabricated in an optimized semiconductor fab, the mismatches in both the optical properties of the pixelated polarization filters and electrical properties of the photodiodes and read-out circuits are minimal, resulting in high accuracy in the reconstructed polarization information for slow rotation rate. Our PDAVIS prototype has larger mismatches between the optical properties of the pixelated filters as well as read-out electronics resulting in larger error at low frequency, which can be mitigated by calibration [23]. However, when the linear polarizer is rotated above ∼100 RPM, the Sony and PDAVIS frames start aliasing and motion blurring (Fig. 2c), which decreases the estimated DoLP and increases the AoP error. The PDAVIS events maintain precise timing information and the reconstructions using events have AoP and DoLP error less than 10° all the way to 1000 RPM.

The second experiment (Fig. 3, Video) assessed the ability to measure time-varying DoLP while DoLP and AoP both vary with time. We combined a rotating linear polarizer with a fixed QWP. Fig. 3a shows how much the DoLP error increases as a function of the speed of the QWP, compared to 30 RPM. For visual comparison, each method is

[3] https://github.com/tylerchen007/firenet-pdavis

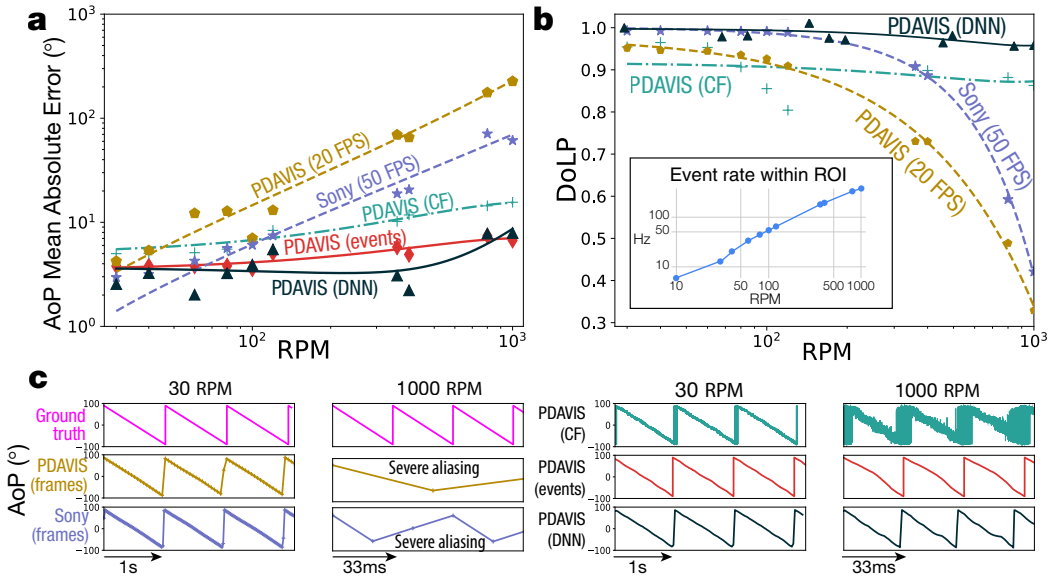

Figure 2. **Comparison of frame-based and event-based AoP and DoLP reconstruction accuracy at various rotational speeds.** Input is image of fully linearly polarized light from a rotating linear polarizer. **a** Mean absolute error (**MAE**) of AoP reconstruction for the various methods averaged over 12x12 Region of Interest (**ROI**) centered on the polarizer. (see Sup. Mat. 3). PDAVIS and Sony frame rates are shown in plots and both exposure durations were fixed to 20 ms. The *frames* methods use only synchronous intensity frames. The CF method fuses 20 FPS frames and events using a method adapted from [29]. The *events* method is illustrated in Fig. 1c. The Deep Neural Network (**DNN**) method uses only events together with the convolutional recurrent neural network [31]. **b** DoLP reconstructions. Both CF or DNN methods show that using events allows reconstructing DoLP well beyond the limiting Nyquist frequency of the frame sampling. Inset plots the event rate per pixel within the polarizer ROI versus RPM; the event rate outside ROI is < 1 Hz after denoising. **c** Reconstruction of the AoP from a 100 pixel ROI using various methods. The frame based Sony and PDAVIS reconstructions are severely aliased at 1000 RPM. which is not true for any of the PDAVIS methods using events.

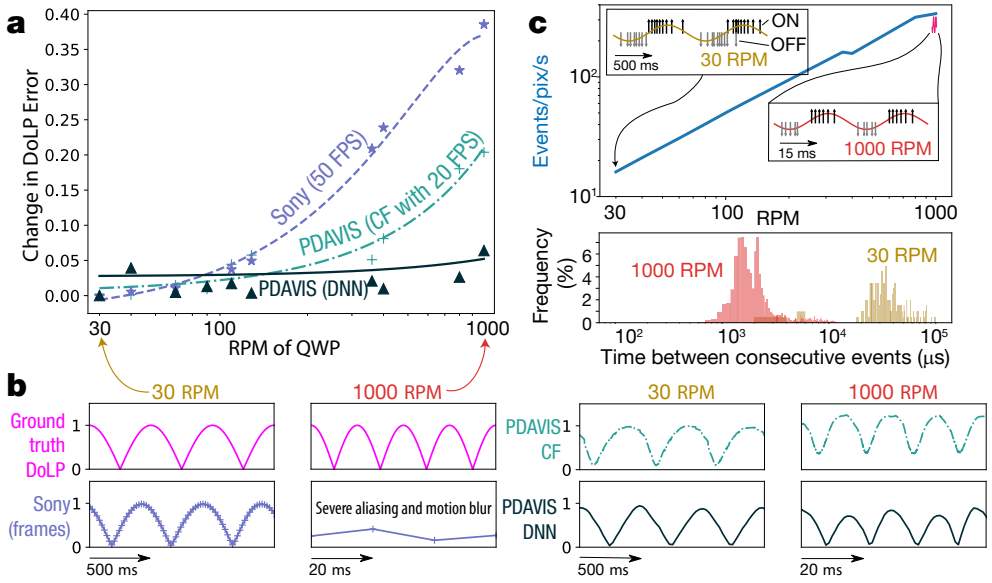

Figure 3. **Comparison of frame-based and event-based reconstruction of DoLP with various rotation speeds of a Quarter Wave Plate (QWP).** Each cycle of QWP rotation produces four cycles of DoLP. **a** Growth of the mean absolute error of DoLP reconstruction with RPM. The Sony has only synchronous intensity frames (see 3.1). The CF method fuses PDAVIS frames and events (see 3.3). The DNN method uses only events (see 3.4). **b** Reconstruction of the absolute DoLP from a 100 pixel ROI using various methods. The frame based Sony reconstruction is most accurate at low frequency but is severely aliased at 1000 RPM, which is not true for any of the PDAVIS methods using events. **c** Statistics of events. Upper plot is event rate versus QWP RPM. Insets show actual ON and OFF events from a subpixel in response to the sinusoidal intensity variation. Lower plot shows histograms of the time between two consecutive events for the two rotational speeds of the QWP.

defined to have zero "change of error" at the lowest frequency. Fig. 3b shows the absolute DoLP measured by each method for 30 and 1000 RPM. At low RPM, the Sony camera makes the most accurate estimate of DoLP. When the QWP is rotated at higher speeds, the frames from both cameras become aliased and motion blurred, resulting in a large error increase of over 50% in the Sony DoLP; at 1000 RPM, the Sony frames are hopelessly blurred and aliased (Fig. 3b, Sony (frames)). However, the CF method fuses the PDAVIS events with its 20 FPS frames, clearly improving the reconstruction in comparison with the 50 FPS Sony (Fig. 3b, PDAVIS CF). Finally, using only the PDAVIS events with the DNN method keeps the growth in reconstruction error below 8% all the way to 1000 RPM (Fig. 3b, PDAVIS DNN). Fig. 3c shows the statistics of the events. At 30 RPM, the distribution of interevent time intervals (lower histogram) shows that the events are widely spaced because the brightness changes are slow. At 1000 RPM, the distribution moves to much shorter event intervals, down to less than 1 ms. The event rate (Fig. 3c upper plot) is directly proportional to RPM. The insets of the event rate plot show events from one pixel; the structure of ON and OFF events is similar for 30 RPM and 1000 RPM, but speeds up by a factor of 30. This low latency asynchronous PDAVIS output allows the measurement of fast brightness changes, which occur much more rapidly than the fixed frame rate; the PDAVIS events sample as needed, up to more than 1 kHz in this experiment.

The third experiment (Fig. 4a, Video) compares the PDAVIS and Sony dynamic range. We imaged set of polarization filters offset by 30°rotating at 200 RPM (5 rev/s) under high contrast 2000:1 lighting, such as commonly encountered in remote sensing of natural environments. The Sony camera exposure is set to 20 ms to capture the darker part of the scene without underexposing it, which overexposes and saturates the brighter part, preventing AoP measurement. The large motion blur is visible in the I0 image and incorrect AoP in the blurred regions. The PDAVIS can measure the AoP in both lighting conditions. Even though the PDAVIS frame is also motion blurred, all event-based methods produce sharp images.

The fourth experiment (Fig. 4b, Video) shows a potential medical imaging application of the PDAVIS. We imaged the dynamics of a bovine tendon subjected to cyclical stress, such that its birefringent properties are time varying. Bovine flexor tendon was sliced using a vibratome to produce 300-micron thick slices. A single sliced tendon is mounted on a 6-Degree of Freedom (**DOF**) computer-controlled actuator and sensor stage. The end pieces of the tendon are clamepd with sandpaper to the sensor stage. An

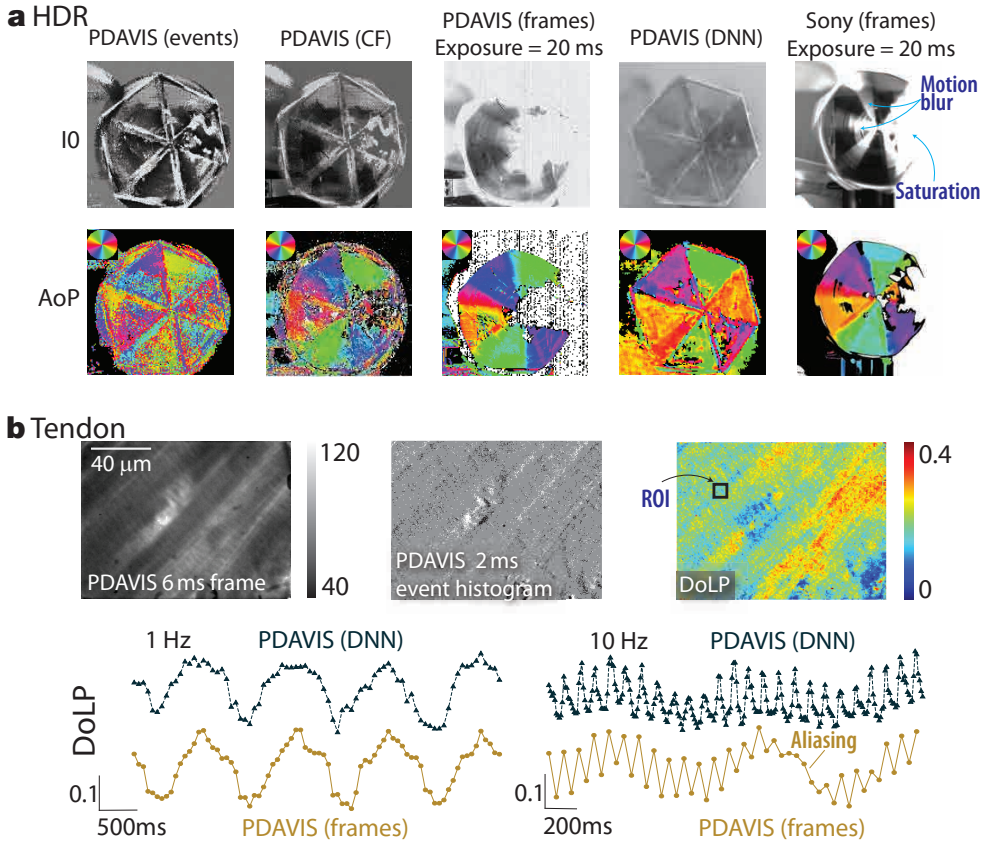

Figure 4. **Applications of PDAVIS for remote sensing and scientific imaging. a** Images of a rotating fan polarizer under HDR illumination captured by the PDAVIS and Sony's camera using various reconstruction methods (see 3). The fan is constructed from triangular linear polarizers arranged with 30° AoP spacing. The illumination ratio between bright and dark parts is 2000 and the rotation speed is 200 RPM. The I_0 images show reconstructed monochromatic intensity from pixels with 0 degree pixelated polarization filters of Fig. 1. The weakly-polarized regions in the AoP images are masked out using the measured DoLP. **b** Imaging a tendon that is periodically stretched at 1 Hz and 10 Hz. The images (upper half) show a single frame (left), an event time window (center) and the corresponding DoLP reconstruction result (right) using the DNN method. The event time window is rendered from a fixed time interval where ON (white) and OFF (black) events are accumulated to the starting gray image. The DNN input is 3D event tensors (the frames are not used) that have a duration of 50 ms or 10 ms, resulting in output at 20 or 100 FPS for 1 Hz and 10 Hz respectively. The traces (lower half) compare the DNN and frame-based reconstructed DoLP, averaged over the ROI indicated in the DoLP image (upper right). With 1 Hz stretching (left), both methods yield similar results. With 10 Hz stretching (right), the DNN reconstructs the DoLP while the 20 FPS frame-based reconstruction is severely aliased.

LED light source combined with a linear polarization filter (Gray Polarizing Film 38-491, Edmund Optics) and an achromatic QWP (AWQP3, Bolder Vision Optik, Boulder, Colorado) were placed under the bovine flexor tendon. This optical setup generates circularly polarized light which is used to illuminate the tendon. The light that is transmitted through the tissue is imaged with either the PDAVIS or Sony polarization sensor. Both sensors were equipped with x10 optical lens with a numerical aperture of 0.25 (f/2) and placed directly above the tissue.

The tendon is cyclically loaded between 2% and 3% strain at rates of 1, 5, and 10 Hz for 30 seconds. During the cyclical loading of the tissue, the birefringent properties of the individual collagen fibers are modulated as a function of the applied strain. As circularly polarized light is transmitted through the tissue under cyclical load, the light passing through the collagen fibers will scatter (*i.e.*, depolarized light) and become elliptically polarized. The ellipticity of the polarized light is directly proportional to the strain applied to the collagen fibers. Hence, the degree of linear polarization provides a measurement of the ellipticity of the circularly polarized light and an indirect measure of the applied strain on the tendon.

Using high optical magnification, we can observe strain patterns over time of the individual collagen fibers that comprise the tendon. Due to the high optical magnification and

rapid movement of the collagen fibers, preventing aliasing would require a frame rate that is a large multiple of the cycle rate. By contrast, DNN reconstruction of the DoLP (using only events) provides measurement of the dynamic properties of the individual collagen fibers at higher frequency than the maximum frame rate.

5. PDAVIS and Sony camera specifications

Table 1 compares the design and measured specifications of the PDAVIS with a state-of-the-art Commodity Off-The-Shelf (**COTS**) frame-based polarization camera (FLIR BFS-U3-51S5), which uses the Sony IMX250 camera chip. Details of our measurements of dynamic range and extinction ratio of PDAVIS precede this section.

The Sony polarization sensor has higher resolution, smaller pixel size, and higher extinction ratio. Our bioinspired sensor is fabricated at several different locations: the event-based sensor is fabricated in a 180nm CIS process provided by TowerJazz Semiconductors; pixelated polarization filters are fabricated in Moxtek cleanroom facilities; the filters and image sensor are integrated at University of Illinois. Due to the complex fabrication steps, the image sensor pixel pitch is larger and the extinction ratios are lower than Sony's sensor. The PDAVIS offers much higher temporal resolution (≈100 us versus 12 ms) and its DVS output has superior DR compared to Sony polarization camera (120dB vs 72dB).

Table 1. Specification and comparison

	PDAVIS (this work)	COTS Sony IMX-250
Tech. Feature size	180nm	90/40nm stacked
Pixel size	18.5μm	3.45μm
Array size	346x260	2448x2048
Output	APS+DVS+IMU	APS
Power (camera)	est. 3 W	3 W
ER at 500nm	40	350
Max APS frame rate	53 Hz[a]	75 Hz
APS DR	52dB [17]	72 dB
Max DVS event rate	10 MHz	-
DVS DR	120dB [17]	-
DVS Min latency	3us@1klux [17]	-
Min DVS threshold[b]	±14%	-
DVS threshold mismatch[c]	3.5% [17]	-

[a] with exposure 80 us.
[b] At room temperature, with mean background leak activity rate of 0.7 Hz with background intensity from APS exposure of 26 DN/ms.
[c] Pixel to pixel 1-σ mismatch of the threshold in temporal contrast.

6. Discussion

Airborne, underwater, and space-based applications can require high temporal resolution and HDR, together with spectral and polarization sensitivity. All of these requirements increase the data rate, but the bioinspired sparse data streams and local gain control of event cameras enables near-sensor processing with low latency and a small computational footprint together with HDR. To compare PDAVIS with state-of-the-art polarization sensors, we developed novel event-driven reconstruction algorithms and compared their angle and degree of polarization reconstruction abilities to the frame-based camera reconstruction. The pure event-driven algorithm is the most economical, but it cannot reconstruct the degree of linear polarization, which requires an estimate of the absolute intensity which the event stream does not provide. The CF helps to overcome this limitation by fusing the event stream with periodically captured frames while only slightly increasing the computational cost. The DNN provides the most accurate reconstruction, but requires a power hungry and expensive GPU for real time operation, which may not be affordable in a remote environment close to the sensor or with minimum latency. A limitation of the PDAVIS is with dense scenes, which can saturate the event output capacity, causing event loss. In these situations, a conventional frame-based polarization camera could be better suited. By adopting a bioinspired combination of sustained and transient pathway, the PDAVIS bridges a gap between the limited temporal and dynamic range of conventional frame-based polarization cameras and complex solid state imagers[33] or streak cameras[34] that can record short sequences at $> 10^7$ FPS. This gap is normally filled by high frame rate cameras that consume a lot of power and demand bright lighting for the short exposure times. The PDAVIS enables continuous AoP and DoLP measurement with high contrast illumination at frequencies several times the Nyquist rate of frame-based image sensors. The PDAVIS event output triggers data acquisition and processing only when needed making it ideally matched with the increasing development of activation-sparsity aware neural accelerators[35]–[37].

7. Funding

Fabrication of the polarization filters and travel was partially funded by the Swiss National Science Foundation Sinergia projects #CRSII5-18O316, #CRSII5-18O316 and ONR Global-X N62909-20-1-2078. This material is based upon research supported by, or in part by, the U. S. Office of Naval Research (N62909-20-1-2078, N00014-19-1-2400 and N00014-21-1-2177) and U.S. Air Force Office of Scientific Research (FA9550-18-1-0278). The authors thank G. Cohen, T. Cronin, and A. Kaneev for comments; C. Scheerlinck for help with implementing the CF; S. Blair and A. Pietros for help with aligning and bonding the polarization filter arrays to the DAVIS sensors; S. Blair, Z. Liang, C. Symons, Y. Chen, and Z. Zhu for help with measurements; S. Blair and Z. Zhu for help with data analysis; and L. Iannucci and S. Lake for assistance with the tendon experiments.

References

[1] T. W. Cronin, S. Johnsen, N. J. Marshall, and E. J. Warrant, *Visual ecology*. Princeton University Press, 2014.

[2] N. J. Marshall, "A unique colour and polarization vision system in mantis shrimps," *Nature*, vol. 333, no. 6173, pp. 557–560, 1988.

[3] G. Horváth, Ed., *Polarized Light and Polarization Vision in Animal Sciences*. Springer, Berlin, Heidelberg, 2014.

[4] A. Altaqui, P. Sen, H. Schrickx, *et al.*, "Mantis shrimp–inspired organic photodetector for simultaneous hyperspectral and polarimetric imaging," *Science Advances*, vol. 7, no. 10, 2021.

[5] M. Garcia, C. Edmiston, R. Marinov, A. Vail, and V. Gruev, "Bio-inspired color-polarization imager for real-time in situ imaging," *Optica*, vol. 4, no. 10, pp. 1263–1271, Oct. 2017.

[6] M. S. Kim, M. S. Kim, G. J. Lee, *et al.*, "Bio-inspired artificial vision and neuromorphic image processing devices," *Advanced Materials Technologies*, vol. n/a, no. n/a, p. 2 100 144,

[7] Y.-J. Jen, A. Lakhtakia, C.-W. Yu, *et al.*, "Biologically inspired achromatic waveplates for visible light," *Nature communications*, vol. 2, no. 1, pp. 1–5, 2011.

[8] C. Liu, C. Shi, T. Wang, *et al.*, "Bio-inspired multimodal 3d endoscope for image-guided and robotic surgery," *Opt. Express*, vol. 29, no. 1, pp. 145–157, Jan. 2021.

[9] S. Blair, M. Garcia, T. Davis, *et al.*, "Hexachromatic bioinspired camera for image-guided cancer surgery," *Science Translational Medicine*, vol. 13, no. 592, 2021, ISSN: 1946-6234.

[10] M. Zhang, X. Wu, N. Cui, N. Engheta, and J. Van der Spiegel, "Bioinspired focal-plane polarization image sensor design: From application to implementation," *Proceedings of the IEEE*, vol. 102, no. 10, pp. 1435–1449, 2014.

[11] M. Sarkar, D. S. S. San Segundo Bello, C. van Hoof, and A. Theuwissen, "Integrated polarization analyzing cmos image sensor for material classification," *IEEE Sensors Journal*, vol. 11, no. 8, pp. 1692–1703, 2011.

[12] T. Tokuda, H. Yamada, K. Sasagawa, and J. Ohta, "Polarization-analyzing cmos image sensor with monolithically embedded polarizer for microchemistry systems," *IEEE Transactions on Biomedical Circuits and Systems*, vol. 3, no. 5, pp. 259–266, 2009.

[13] W.-L. Hsu, G. Myhre, K. Balakrishnan, N. Brock, M. Ibn-Elhaj, and S. Pau, "Full-stokes imaging polarimeter using an array of elliptical polarizer," *Opt. Express*, vol. 22, no. 3, pp. 3063–3074, Feb. 2014.

[14] S. B. Powell, R. Garnett, J. Marshall, C. Rizk, and V. Gruev, "Bioinspired polarization vision enables underwater geolocalization," *Science Advances*, vol. 4, no. 4, 2018.

[15] N. J. Marshall, S. B. Powell, T. W. Cronin, *et al.*, "Polarisation signals: A new currency for communication," *Journal of Experimental Biology*, vol. 222, no. 3, 2019.

[16] R. N. Patel and T. W. Cronin, "Mantis shrimp navigate home using celestial and idiothetic path integration," *Current Biology*, vol. 30, no. 11, 1981–1987.e3, 2020, ISSN: 0960-9822.

[17] C. Brandli, R. Berner, M. Yang, S.-C. Liu, and T. Delbruck, "A 240×180 130 dB 3 μs latency global shutter spatiotemporal vision sensor," *IEEE Journal of Solid-State Circuits*, vol. 49, no. 10, pp. 2333–2341, 2014.

[18] G. Gallego, T. Delbruck, G. M. Orchard, *et al.*, "Event-based vision: A survey," *IEEE Trans. Pattern Anal. Mach. Intell.*, vol. PP, pp. 1–1, Jul. 2020, ISSN: 0162-8828.

[19] J. S. Tyo, D. L. Goldstein, D. B. Chenault, and J. A. Shaw, "Review of passive imaging polarimetry for remote sensing applications," *Applied optics*, vol. 45, no. 22, pp. 5453–5469, 2006.

[20] N. A. Rubin, G. D'Aversa, P. Chevalier, Z. Shi, W. T. Chen, and F. Capasso, "Matrix fourier optics enables a compact full-stokes polarization camera," *Science*, vol. 365, no. 6448, eaax1839, 2019.

[21] R. Azzam, "Division-of-amplitude photopolarimeter (doap) for the simultaneous measurement of all four stokes parameters of light," *Optica Acta: International Journal of Optics*, vol. 29, no. 5, pp. 685–689, 1982.

[22] M. Muglikar, L. Bauersfeld, D. P. Moeys, and D. Scaramuzza, "Event-based shape from polarization," *arXiv preprint arXiv:2301.06855*, 2023.

[23] V. Gruev, R. Perkins, and T. York, "CCD polarization imaging sensor with aluminum nanowire optical filters," *Optics express*, vol. 18, no. 18, pp. 19 087–19 094, 2010.

[24] T. York, R. Marinov, and V. Gruev, "260 frames-per-second 648x488 resolution division-of-focal-plane polarimeter with structural dynamics and tracking applications," *Optics express*, vol. 24, no. 8, pp. 8243–8252, 2016.

[25] E. Arbabi, S. M. Kamali, A. Arbabi, and A. Faraon, "Full-stokes imaging polarimetry using dielectric metasurfaces," *Acs Photonics*, vol. 5, no. 8, pp. 3132–3140, 2018.

[26] Y. Maruyama, T. Terada, T. Yamazaki, *et al.*, "3.2-mp back-illuminated polarization image sensor with four-directional air-gap wire grid and 2.5 micron pixels," *IEEE Transactions on Electron Devices*, vol. 65, no. 6, pp. 2544–2551, 2018.

[27] E. Collett, *Field guide to polarization*. spie.org, 2005, ISBN: 9780819458681.

[28] C. Brandli, L. Muller, and T. Delbruck, "Real-Time, High-Speed video decompression using a frame- and Event-Based DAVIS sensor," in *Proc. 2014 Intl. Symp. Circuits and Systems (ISCAS 2014)*, Melbourne, Australia, 2014, pp. 686–689.

[29] C. Scheerlinck, N. Barnes, and R. Mahony, "Continuous-Time intensity estimation using event cameras," in *Computer Vision – ACCV 2018*, Springer International Publishing, 2019, pp. 308–324.

[30] Y. Nozaki and T. Delbruck, "Temperature and parasitic photocurrent effects in dynamic vision sensors," *IEEE Trans. Electron Devices*, vol. 64, no. 8, pp. 3239–3245, Aug. 2017, ISSN: 0018-9383, 1557-9646.

[31] C. Scheerlinck, H. Rebecq, D. Gehrig, N. Barnes, R. Mahony, and D. Scaramuzza, "Fast image reconstruction with an event camera," in *Proceedings of the IEEE/CVF Winter Conference on Applications of Computer Vision*, 2020, pp. 156–163.

[32] H. Rebecq, R. Ranftl, V. Koltun, and D. Scaramuzza, "High speed and high dynamic range video with an event camera," *IEEE Trans. Pattern Anal. Mach. Intell.*, vol. 43, no. 6, pp. 1964–1980, Jun. 2021, ISSN: 0162-8828.

[33] T. G. Etoh, V. T. S. Dao, H. D. Nguyen, *et al.*, "R57 progress of ultra-high-speed image sensors with in-situ CCD storage," in *2011 INTERNATIONAL IMAGE SENSOR WORKSHOP*, Intl. Image Sensor Society, 2011.

[34] L. Gao, J. Liang, C. Li, and L. V. Wang, "Single-shot compressed ultrafast photography at one hundred billion frames per second," *Nature*, vol. 516, no. 7529, pp. 74–77, Dec. 2014, ISSN: 0028-0836, 1476-4687.

[35] M. Davies, N. Srinivasa, T. Lin, *et al.*, "Loihi: A neuromorphic manycore processor with On-Chip learning," *IEEE Micro*, vol. 38, no. 1, pp. 82–99, Jan. 2018, ISSN: 1937-4143.

[36] Y.-H. Chen, T. Krishna, J. S. Emer, and V. Sze, "Eyeriss: An Energy-Efficient reconfigurable accelerator for deep convolutional neural networks," *IEEE J. Solid-State Circuits*, vol. 52, no. 1, pp. 127–138, Jan. 2017, ISSN: 0018-9200, 1558-173X.

[37] A. Aimar, H. Mostafa, E. Calabrese, *et al.*, "NullHop: A flexible convolutional neural network accelerator based on sparse representations of feature maps," *IEEE Trans Neural Netw Learn Syst*, Jul. 2018, ISSN: 2162-2388, 2162-237X.